Fluid Dynamics Research 32 (2003) 261–281

FLUID DYNAMICS RESEARCH

# Nonparallel stability of the flow in an axially rotating pipe

C. del Pino*, J. Ortega-Casanova, R. Fernandez-Feria

*Universidad de Malaga, E.T.S. Ingenieros Industriales, 29013 Malaga, Spain*

Received 16 December 2002; received in revised form 10 April 2003; accepted 22 April 2003
Communicated by T. Mullin

**Abstract**

The linear stability of the developing flow in an axially rotating pipe is analyzed using parabolized stability equations (PSE). The results are compared with those obtained from a near-parallel stability approximation that only takes into account the axial variation of the basic flow. Though the PSE results obviously coincide with the near-parallel ones far downstream, when the flow has reached a Hagen-Poiseuille axial velocity profile with superimposed solid-body rotation, they differ significantly in the developing region. Therefore, the onset of instability strongly depends on the axial evolution of the perturbations. The PSE results are also compared with experimental data from Imao et al. [Exp. Fluids 12 (1992) 277], showing a good agreement in the frequencies and wavelengths of the unstable disturbances, that take the form of spiral waves. Finally, a simple method for detecting one of the conditions to characterize the onset of absolute instability using PSE is given.



*PACS:* 47.20.−k; 47.30.+s; 47.60.+i

*Keywords:* Hydrodynamic stability; PSE; Rotating pipe flow

## 1. Introduction

The linear stability of fully developed Hagen-Poiseuille flow with superimposed solid-body rotation has been considered by several authors (Pedley, 1969; Maslowe, 1974; Mackrodt, 1976; Cotton and Salwen, 1981; Maslowe and Stewartson, 1982; Fernandez-Feria and del Pino, 2002). Although it is to be expected that in an axially rotating pipe, if the flow is steady, Poiseuille flow plus solid-body rotation will be the ultimate form of the motion far downstream, these theoretical stability results are not easily tested experimentally because, as it was first argued by Pedley (1969), this ultimate

* Corresponding author. Tel.: +34-952-132756; fax: +34-952-132691.
*E-mail address:* cpino@uma.es (C. del Pino).

0169-5983/03/$30.00 
doi:10.1016/S0169-5983(03)00067-4

form is reached too far downstream: the length of the pipe has to be, at least, the maximum of $Re \times R$ or $ReL \times R$, where $R$ is the radius of the pipe, $Re$ is the axial Reynolds number, and $L$ is the swirl parameter (see next section for a precise definition of these two-nondimensional parameters). Actually, Pedley showed that earlier experiments by White (1964) did not satisfy this criterium. In addition, another important difficulty is the fact that, for Reynolds numbers and swirl parameters above their critical values for stability, the flow may become unstable in the developing region before the Poiseuille axial flow and the solid-body rotation are both fully developed, so that this ultimate form of the flow is never reached in practice. That this is what actually happens was shown by Imao et al. (1992), who performed accurate LDA measurements of the flow in an axially rotating pipe when an uniform flow is introduced therein, for a given $Re$ and a wide range of values of $L$. These authors pointed out that spiral instability waves appeared clearly in the transition region for high enough values of the rotation rate of the pipe.

To shed some new light into this problem, in the present paper we analyze the nonparallel linear stability of the flow in an axially rotating pipe when an uniform flow with no rotation is introduced at the inlet. The structure of the paper is the following: in Section 2, numerical results are given for the basic flow, i.e. for the axisymmetric developing flow in an axially rotating pipe with an uniform flow at the inlet. We use a streamfunction-vorticity-circulation formulation for the numerical simulation, in a pipe of length large enough to reach the desired final Poiseuille axial flow with superimposed solid-body rotation. It must be noted here that this ultimate downstream flow can always be reached with an axisymmetric numerical simulation because the asymptotic flow is stable to axisymmetric perturbations for all values of $Re$ and $L$ Mackrodt, 1976; Cotton and Salwen, 1981; Fernandez-Feria and del Pino, 2002). The nonparallel linear stability of this flow is analyzed using the parabolized stability equations (PSE) technique (Bertolotti et al., 1992; Herbert, 1997) which takes into account both the axial evolution of the basic flow and the axial history of the perturbations. The formulation of this stability problem is given in Section 3. In Section 4 we compare the results of the PSE both with near-parallel stability results that only consider the axial variation of the basic flow, and with the experimental results of Imao et al. (1992). We also analyze the onset of absolute instability. Finally, Section 5 discusses these results, showing the great advantages of the PSE over the near-parallel approximation, and its appropriateness to characterize not only the appearance of convective instabilities, but also the onset of absolute instability in this kind of flow.

## 2. Axisymmetric developing flow in an axially rotating pipe

The basic flow whose stability is going to be considered here consists on an axisymmetric flow in an axially rotating pipe of radius $R$ with angular velocity $\Omega$. At the inlet, the flow is assumed uniform with axial velocity $W_i$. If the pipe is long enough, the flow tends to an axial Poiseuille flow plus solid-body rotation. In cylindrical polar coordinates $(r, \theta, z)$, this far downstream flow has a velocity field given by

$$\mathbf{V} \equiv [U, V, W] = W_0[0, Ly, (1 - y^2)], \tag{1}$$

where

$$y \equiv \frac{r}{R}, \tag{2}$$

is the nondimensional radial distance, $W_0 = 2W_i$ is the maximum axial velocity at the axis and $L$ is the swirl parameter,

$$L \equiv \frac{\Omega R}{W_0}. \tag{3}$$

The other two dimensionless parameters governing the flow are the Reynolds number

$$Re \equiv \frac{W_0 R}{\nu} = \frac{2W_i R}{\nu}, \tag{4}$$

where $\nu$ is the kinematic viscosity, and the aspect ratio

$$\Delta = \frac{R}{z_0}, \tag{5}$$

where $z_0$ is the pipe length (the nondimensional pipe length $\Delta^{-1}$ is a large parameter). It is also convenient to define a Reynolds number for the azimuthal flow, $Re_\theta \equiv \Omega R^2/\nu = ReL$.

The numerical simulation of this flow has been considered by Imao et al. (1989), among others. Here we use the streamfunction-vorticity-circulation formulation, where the nondimensional stream function $\Psi$, vorticity $\eta$, and circulation $\Gamma$ are defined, respectively, through

$$\frac{U}{W_0} = -\frac{\Delta}{y}\frac{\partial \Psi}{\partial x}, \quad \frac{W}{W_0} = \frac{1}{y}\frac{\partial \Psi}{\partial y}, \tag{6}$$

$$\eta = \frac{R}{W_0}[\nabla \wedge \mathbf{V}]_\theta = \frac{\Delta}{W_0}\frac{\partial U}{\partial x} - \frac{1}{W_0}\frac{\partial W}{\partial y}, \tag{7}$$

$$\Gamma = y\frac{V}{W_0}, \tag{8}$$

where

$$x \equiv \frac{z}{z_0}, \tag{9}$$

is the nondimensional axial coordinate. With this formulation, the continuity equation is satisfied identically, and the three equations to be solved are the azimuthal components of the momentum and the vorticity equations, together with definition (7) of $\eta$. These nondimensional equations can be written as

$$\frac{\partial \Gamma}{\partial t} = \frac{1}{y}\frac{\partial \Psi}{\partial x}\frac{\partial \Gamma}{\partial y} - \frac{1}{y}\frac{\partial \Psi}{\partial y}\frac{\partial \Gamma}{\partial x} + \frac{1}{Re\Delta}\left(\frac{\partial^2 \Gamma}{\partial y^2} - \frac{1}{y}\frac{\partial \Gamma}{\partial y} + \Delta^2\frac{\partial^2 \Gamma}{\partial x^2}\right), \tag{10}$$

$$\frac{\partial \eta}{\partial t} = \frac{1}{y}\frac{\partial \Psi}{\partial x}\frac{\partial \eta}{\partial y} - \frac{1}{y}\frac{\partial \Psi}{\partial y}\frac{\partial \eta}{\partial x} - \frac{\eta}{y^2}\frac{\partial \Psi}{\partial x} + \frac{\Gamma}{y^3}\frac{\partial \Gamma}{\partial x} + \frac{1}{Re\Delta}\left(\frac{\partial^2 \eta}{\partial y^2} + \frac{1}{y}\frac{\partial \eta}{\partial y} - \frac{\eta}{y^2} + \Delta^2\frac{\partial^2 \eta}{\partial x^2}\right), \tag{11}$$

$$\frac{\partial^2 \Psi}{\partial y^2} - \frac{1}{y}\frac{\partial \Psi}{\partial y} + \Delta^2\frac{\partial^2 \Psi}{\partial x^2} = -y\eta. \tag{12}$$

Note that $\Psi$, $\eta$, $\Gamma$, and the time $t$ are made dimensionless with $W_0R^2$, $W_0/R$, $W_0R$, and $z_0/W_0$, respectively.

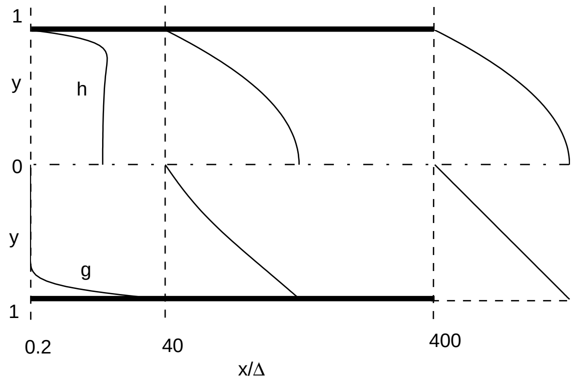


Fig. 1. Sketch of the pipe geometry, together with steady state radial velocity profiles of the axial velocity $h$ (upper curves) and azimuthal velocity $g$ (lower curves) at $x/\Delta = 0.2, 40$, and 400. $\Delta^{-1} = 400$, $Re = 500$ and $L = 0.5$. The numerical computations are obtained using $\delta x = 5\times 10^{-4}$, $\delta y = 0.012$, and $\delta t = 10^{-4}$. The steady-state plotted corresponds to $t \simeq 143$.

These equations are solved with the following boundary conditions (see Fig. 1 for a sketch of the geometry): At the inlet, $x = 0$, we assume an uniform axial velocity profile together with $U = V = 0$,

$$\Psi = y^2, \quad \eta = -\frac{\Delta^2}{y}\frac{\partial^2\Psi}{\partial x^2}, \quad \Gamma = 0 \quad \text{at } x = 0,\ 0 \leqslant y \leqslant 1. \tag{13}$$

At the pipe exit, $x = 1$, the velocity profiles are assumed to be independent of $x$,

$$\frac{\partial^2\Psi}{\partial x^2} = 0, \quad \eta = -\frac{1}{y}\frac{\partial^2\Psi}{\partial y^2} - \frac{1}{y^2}\frac{\partial\Psi}{\partial y}, \quad \frac{\partial\Gamma}{\partial x} = 0 \quad \text{at } x = 1, \quad 0 \leqslant y \leqslant 1. \tag{14}$$

At the axis of symmetry, we have

$$\Psi = \eta = \Gamma = 0 \quad \text{at } 0 \leqslant x \leqslant 1, \quad y = 0. \tag{15}$$

Finally, at the solid rotating wall, $U = W = 0$ and $V/W_0 = L$

$$\Psi = 0, \quad \eta = -\frac{1}{y}\frac{\partial^2\Psi}{\partial y^2}, \quad \Gamma = L \quad \text{at } 0 \leqslant x \leqslant 1, \quad y = 1. \tag{16}$$

In the computations we have selected a pipe length $\Delta^{-1}$ large enough to reach, in the steady state, the flow (1) downstream, which in the present variables is given by

$$[\Psi, \eta, \Gamma] = [y^2/2 - y^4/4, 2y, Ly]. \tag{17}$$

As estimated by Pedley (1969), $\Delta^{-1} = O[\max(Re, Re_\theta)]$. However, we found in the different simulations shown in this paper that Pedley's criterion is really conservative. The asymptotic downstream flow is reached with just 30 or 40 percent of that estimated length. This is also observed in the experimental results given by Imao et al. (1992). For the most unfavorable case considered, $Re = 500$ and $L = 1.5$, for which the estimated pipe length would be $\Delta^{-1} \approx 750$, the asymptotic downstream flow is already reached at $z/R \approx 360$ both, in the experiments and in the numerical simulations. For this reason we have selected $\Delta^{-1} = 400$ in all the simulations given below.

To solve problem (10)–(16) numerically we have used an explicit finite difference scheme, with second-order differences in space, and a second-order predictor–corrector method to advance in time (see, e.g., Lopez and Weidman, 1996). For given values of $Re$ and $L$, the computation starts at $t=0$ with the fluid at rest, and ends when a steady state is reached. Once the steady basic flow in the variables $[\Psi(y,x),\eta(y,x),\Gamma(y,x)]$ is found, Eqs. (6) and (8) are used to obtain the velocity field, which in dimensionless variables will be written as $[f(y,x),g(y,x),h(y,x)]$, related to $[U,V,W]$ by

$$\mathbf{V}\equiv W_0[\Delta f, Lg, h]. \tag{18}$$

As we shall see in the next section, the pressure field of the basic flow, which can of course also be obtained from $[\Psi,\eta,\Gamma]$ by solving an additional Poisson equation, is not needed in the linear stability analysis of the flow due to the fact that the pressure enters linearly into the momentum equations. The possibility of getting rid of the pressure field is thus one of the reasons why we have used the simpler $\Psi-\eta-\Gamma$ formulation to solve numerically the incompressible basic flow. (However, the stability problem of the following sections is best described in primitive velocity–pressure variables.) Fig. 1 shows some radial profiles of the steady-state axial ($h$) and azimuthal ($g$) velocity components at several axial locations for $Re=500$ and $L=0.5$ ($\Delta^{-1}=400$).

## 3. Nonparallel linear stability formulation

### 3.1. Parabolized stability equations

The nonparallel stability of the flow in an axially rotating pipe described above is now analyzed using PSE. The flow variables, $(u,v,w)$ and $p$, are decomposed into their mean parts, $(U,V,W)$ and $P$, and small perturbations. Following (18),

$$u=W_0(\Delta f+\bar{u}), \tag{19}$$

$$w=W_0(h+\bar{w}), \tag{20}$$

$$v=W_0(Lg+\bar{v}), \tag{21}$$

$$p=\rho W_0^2(e+\bar{p}), \tag{22}$$

where $\rho$ is the fluid density, and $e(y,x)$ is the nondimensional pressure field of the basic flow ($P\equiv\rho W_0^2 e$). As we shall see below, $e$ does not enter explicitly into the linear stability equations. The nondimensional small perturbations,

$$\mathbf{s}\equiv[\bar{u},\bar{v},\bar{w},\bar{p}] \tag{23}$$

which, in general, are functions of the four independent (nondimensional) variables $(y,\theta,x,t)$, are decomposed in the standard form (Bertolotti et al., 1992)

$$\mathbf{s}(y,\theta,x,t)=\mathbf{S}(y,x)\chi(x,\theta,t). \tag{24}$$

The complex amplitude

$$\mathbf{S}(y,x) \equiv [F(y,x), G(y,x), H(y,x), \Pi(y,x)], \tag{25}$$

is allowed to depend on the axial co-ordinate $x$, in addition to the radial one, to account for the nonparallelism of the basic flow. The other part of the perturbation is an exponential that describes the wave-like nature of the disturbances,

$$\chi(x,\theta,t) = \exp\left[\frac{1}{\Delta}\int_{x_0}^{x} a(x')\,\mathrm{d}x' + \mathrm{i}n\theta - \mathrm{i}\omega\frac{t}{\Delta}\right], \tag{26}$$

where $x_0$ is the axial point in which the disturbances are introduced, $a(x)$ is the nondimensional (complex) axial wavenumber, $n$ is the azimuthal wave number, and $\omega$ is the nondimensional frequency of the disturbances. $a$ and $\omega$ are defined as

$$a \equiv \mathrm{i}\hat{k}R \equiv \gamma + \mathrm{i}\alpha, \tag{27}$$

$$\omega \equiv \frac{\hat{\omega}R}{W_0}, \tag{28}$$

where $\hat{k}$ and $\hat{\omega}$ are the dimensional frequency and axial wavenumber, respectively. The real part of $a(x)$, $\gamma(x)$, is the exponential growth rate, and its imaginary part, $\alpha(x)$, is the axial wavenumber. In the spatial stability analysis to be considered here, one fixes a real frequency $\omega$ and looks for complex values of $a(x)$. The flow is unstable when $\gamma(x) > 0$.

Substituting (19)–(28) into the incompressible Navier–Stokes equations and neglecting second-order terms in both the small perturbations (i.e., linear stability), and $\Delta$ (i.e., neglecting terms with second order axial derivatives, which constitutes the basis of the PSE technique; see, e.g., Bertolotti et al., 1992; Herbert, 1997) one obtains the following parabolic stability equation for $\mathbf{S}$:

$$\mathbf{L}\cdot\mathbf{S} + \Delta\mathbf{M}\cdot\frac{\partial\mathbf{S}}{\partial x} = \mathbf{0}. \tag{29}$$

The matrix operators $\mathbf{L}$ and $\mathbf{M}$ are defined as follows:

$$\mathbf{L} \equiv \mathbf{L}_1 + a\mathbf{L}_2 + \frac{1}{Re}\mathbf{L}_3 + a^2\frac{1}{Re}\mathbf{L}_4 + \Delta\mathbf{L}_5, \tag{30}$$

$$\mathbf{L}_1 = \begin{pmatrix} 1 + y\frac{\partial}{\partial y} & \mathrm{i}n & 0 & 0 \\ \mathrm{i}(nLg - \omega y) & -2Lg & 0 & y\frac{\partial}{\partial y} \\ L(y\frac{\partial g}{\partial y} + g) & \mathrm{i}(nLg - \omega y) & 0 & \mathrm{i}n \\ y\frac{\partial h}{\partial y} & 0 & \mathrm{i}(nLg - \omega y) & 0 \end{pmatrix}, \tag{31}$$

$$\mathbf{L}_2 = \mathbf{M} = \begin{pmatrix} 0 & 0 & y & 0 \\ yh & 0 & 0 & 0 \\ 0 & yh & 0 & 0 \\ 0 & 0 & yh & y \end{pmatrix}, \quad \mathbf{L_4} = \begin{pmatrix} 0 & 0 & 0 & 0 \\ -y & 0 & 0 & 0 \\ 0 & -y & 0 & 0 \\ 0 & 0 & -y & 0 \end{pmatrix}, \tag{32}$$

$$\mathbf{L}_3 = \begin{pmatrix} 0 & 0 & 0 & 0 \\ -D_y + \frac{n^2+1}{y} & \frac{2in}{y} & 0 & 0 \\ -\frac{2in}{y} & -D_y + \frac{n^2+1}{y} & 0 & 0 \\ 0 & 0 & -D_y + \frac{n^2}{y} & 0 \end{pmatrix}, \quad D_y \equiv y\frac{\partial^2}{\partial y^2} + \frac{\partial}{\partial y}, \tag{33}$$

$$\mathbf{L}_5 = \begin{pmatrix} 0 & 0 & 0 & 0 \\ y\frac{\partial f}{\partial y} + f\frac{\partial}{\partial y} & 0 & 0 & 0 \\ 0 & f(1 + y\frac{\partial}{\partial y}) & Ly\frac{\partial g}{\partial x} & 0 \\ 0 & 0 & y(\frac{\partial h}{\partial x} + f\frac{\partial}{\partial y}) & 0 \end{pmatrix}. \tag{34}$$

This equation has to be solved with the following boundary conditions at the axis $y = 0$ (e.g. Batchelor and Gill, 1962), and at the pipe wall $y = 1$:

$$F(0,x) = G(0,x) = 0, \quad \mathrm{d}H/\mathrm{d}y|_{y=0} = 0, \quad (n = 0), \tag{35}$$

$$F(0,x) \pm \mathrm{i}G(0,x) = 0, \quad \mathrm{d}F/\mathrm{d}y|_{y=0} = 0, \quad H(0,x) = 0, \quad (n = \pm 1), \tag{36}$$

$$F(0,x) = G(0,x) = H(0,x) = 0, \quad (|n| > 1); \tag{37}$$

$$F(1,x) = G(1,x) = H(1,x) = 0. \tag{38}$$

It also needs an *initial* condition at $x = x_0$. A convenient choice is the solution of the local eigenvalue problem (Bertolotti et al., 1992; Fernandez-Feria, 1999)

$$\mathbf{L}_0 \cdot \mathbf{S}_0 \equiv \left[\mathbf{L}_1 + a_0\mathbf{L}_2 + \frac{1}{Re}\mathbf{L}_3 + a_0^2\frac{1}{Re}\mathbf{L}_4 + \Delta\mathbf{L}_5\right] \cdot \mathbf{S}_0 = \mathbf{0}, \tag{39}$$

that provides the initial eigenvalue $a_0 \equiv a(x_0)$, and eigenfunction $\mathbf{S}_0(y) \equiv \mathbf{S}(y, x_0)$, which will be used to start the axial integration of Eq. (29) for a given set of nondimensional parameters. Note that for the spatial stability analysis that we are considering here (real frequency $\omega$ and complex wavenumber $a_0$, which is the appropriate one for a stability analysis based on the PSE; Bertolotti et al., 1992), Eq. (39) with boundary conditions (35)–(38) constitute a nonlinear eigenvalue problem. For a parallel basic flow like a Hagen-Poiseuille flow plus solid-body rotation [i.e., when (18) is given by (1)], this problem coincides with that considered in Fernandez-Feria and del Pino (2002).

Eq. (39) accounts for the effect of the nonparallelism of the basic flow, but neglects the effect of the history or convective evolution of the perturbations. Its solution for different values of $x > x_0$ will be compared in the next section with the solution to the PSE (29) to measure the importance of this last effect. This local solution will be termed near-parallel (NP) solution.

### 3.2. Normalization condition and numerical method

As it stands, there is some ambiguity in the partition of the perturbations (24) into two functions of $x$. To close the problem one has to enforce an additional condition which puts some restriction on the axial variation of $\mathbf{S}$. Basically, one uses a normalization condition that restricts rapid changes in $x$ of $\mathbf{S}$, according to the slow axial variation of the basic flow (small $\Delta$). Thus, the growth rate and the axial sinusoidal variation are represented by the exponential function $\chi$. Several types of normalization conditions can be used (Bertolotti et al., 1992; Herbert, 1997; Fernandez-Feria, 1999). Here we will use an integral condition based on the kinetic energy of the perturbations. Defining a physical amplification rate $a_1$ based on the axial variation of the kinetic energy of the perturbations

$$a_1(x) \equiv \gamma_1(x) + \mathrm{i}\alpha_1(x) \equiv R\frac{\int_0^R [\bar{u}^{\,\dagger}(\partial\bar{u}/\partial z) + \bar{v}^{\dagger}(\partial\bar{v}/\partial z) + \bar{w}^{\dagger}(\partial\bar{w}/\partial z)]\,\mathrm{d}r}{\int_0^R [|\bar{u}|^2 + |\bar{v}|^2 + |\bar{w}|^2]\,\mathrm{d}r}$$

$$= a(x) + \Delta\frac{\int_0^1 [F^{\dagger}(\partial F/\partial x) + G^{\dagger}(\partial G/\partial x) + H^{\dagger}(\partial H/\partial x)]\,\mathrm{d}y}{\int_0^1 [|F|^2 + |G|^2 + |H|^2]\,\mathrm{d}y}, \tag{40}$$

where † denotes the complex conjugate, the normalization condition used here can be expressed as $a_1(x) = a(x)$ for all $x > x_0$. That is, at each axial step in the integration of (29), the second term in the right-hand side of (40) (the one multiplied by $\Delta$) is set equal to zero, transferring the main part of the streamwise variation of the perturbations to the exponential function $\chi$.

To solve numerically Eq. (29) together with its normalization condition, the radial ($y$) dependence of $\mathbf{S}$ is discretized using a staggered Chebyshev spectral collocation technique (Khorrami et al., 1989). This method has the advantage of eliminating the requirement of two artificial pressure boundary conditions at $y = 0$ and 1 which, for that reason, are not included in (35)–(38). To implement the spectral numerical method, Eq. (29) is discretized by expanding $\mathbf{S}$ in terms of truncated Chebyshev series. The Chebyshev polynomials domain $-1 \leqslant s \leqslant 1$ is mapped into the radial interval $0 \leqslant y \leqslant 1$ using $y = (s+1)/2$. This simple transformation concentrates the Chebyshev collocation points at both the axis and the pipe wall. Cubic splines are used to adapt the numerical solution of the basic flow to the Chebyshev collocation points. The radial domain is thus discretized in $N$ points, $N$ being the number of Chebyshev polynomials in which $\mathbf{S} = [F, G, H, \Pi]$ has been expanded. The number of points $N$ is 50 in all the results presented here. The accuracy of these results has been checked by comparing them with those obtained using higher values of $N$.

The streamwise variation of (29) is solved numerically using an implicit finite difference scheme:

$$\mathbf{L}_{j+1} \cdot \mathbf{S}_{j+1} + \Delta\mathbf{M} \cdot \frac{\mathbf{S}_{j+1} - \mathbf{S}_j}{(\delta x)_j} = \mathbf{0}, \tag{41}$$

where $j$ is the step index in the axial direction, and $(\delta x)_j$ the step size. A marching technique is used to solve the $4N$ discretized equations resulting from (41), starting at $x = x_0$. Since the unknown $a$ appears with $\mathbf{S}$, this equation constitutes, together with the normalization condition, a system of nonlinear equations for $\mathbf{S}$ and $a$. Iteration is used to solve the nonlinear system of discretized algebraic equations at each axial station $j+1$: one starts with the results of the previous station $j$, and uses (41) with $a_j$ to obtain a first approximation for $\mathbf{S}_{j+1}$; these are used in the normalization condition to yield a first approximation for $a_{j+1}$, which is again used to correct $\mathbf{S}_{j+1}$; the iteration procedure is continued until the modifications in the real and imaginary parts of $a$ are both less than $10^{-8}$. Usually, between 2 and 4 iterations were needed (except in the first step after $x = x_0$, where more iterations are required). The process is repeated at the next marching step. Numerical instability puts a lower limit to the axial step size $(\delta x)_j$ for given values of the physical parameters and of those for given $N$. This limitation strongly affects the axial accuracy of the function $a(x)$ obtained numerically. To have some control on the numerical instability we have used the technique described by Anderson et al. (1998), which allows the use of smaller step sizes $\delta x$ in numerically stable schemes and, consequently, improving the axial accuracy of the solution. Thanks to this method we can reach values of $\delta x$ small enough to obtain $a(x)$ with four or five significant figures.

As mentioned above, the initial condition of (29) and its normalization condition at $x = x_0$, $\mathbf{S}_0$ and $a_0$, are the eigenfunctions and eigenvalues of Eq. (39). This is a nonlinear eigenvalue problem, which is solved using the linear companion matrix method described by Bridges and Morris (1984). The resulting (complex) linear eigenvalue problem of dimension $8N$ is solved with the IMSL subroutine DGVCCG, which provides the entire eigenvalue and eigenvector spectrum. Owing to nonlinearity, the size of the matrices in the spatial eigenvalue problem is thus twice the size of the matrices in the radial discretization of (41), so that the computation time to obtain the initial condition is much larger that the computation time of marching with the PSE. Also, due to the large dimension of the matrices in (39), a relatively large amount of spurious numerical eigenvalues with very small wavenumbers (large wavelengths) are produced by the eigenvalue solver. They are easily discarded, however, because the corresponding growth rates increase without bound with $N$, instead of rapidly converging to a finite value as $N$ is increased, as it happens for eigenvalues of physical modes. Finally, to mention that the PSE solution started with the local eigensolution presents a short transient of typically a few $\delta x$ before converging to the actual solution of the PSE.

## 4. Stability results and discussion

### 4.1. Comparison between near-parallel and PSE results

As just stated, the eigenvalues and eigenfunctions of Eq. (39) at some initial axial location $x = x_0$ will be used as the initial values of the PSE (29). Before characterizing the stability properties of the flow with that equation, it is of interest to compare the function $a(x)$ obtained from (39) in the whole range $x_0 \leqslant x \leqslant 1$ with the corresponding PSE results.

Fig. 2 shows this comparison for $Re = 100$ and $L = 0.5$, when the disturbance frequency is $\omega = -1$, and the azimuthal wavenumber is $n = -1$ (the pipe length selected is $\Delta^{-1} = 100$). The corresponding far downstream Hagen-Poiseuille flow plus solid-body rotation is stable for these perturbations (actually, the asymptotic flow for these values of $Re$ and $L$ is linearly stable for any perturbation). Therefore, it is expected that $\gamma(x) < 0$ for every value of $x$. This is shown to be the case in Fig. 2, where we plot the functions $\gamma_{NP}(x)$ and $\alpha_{NP}(x)$ for $x_0 = 0.015 \leqslant x \leqslant 1$ obtained from the near-parallel approximation (39) for the three lest stable modes (lines with circles). It is observed that the less stable mode at $x = x_0$ (largest $\gamma$) becomes the most stable (smaller $\gamma$) of the

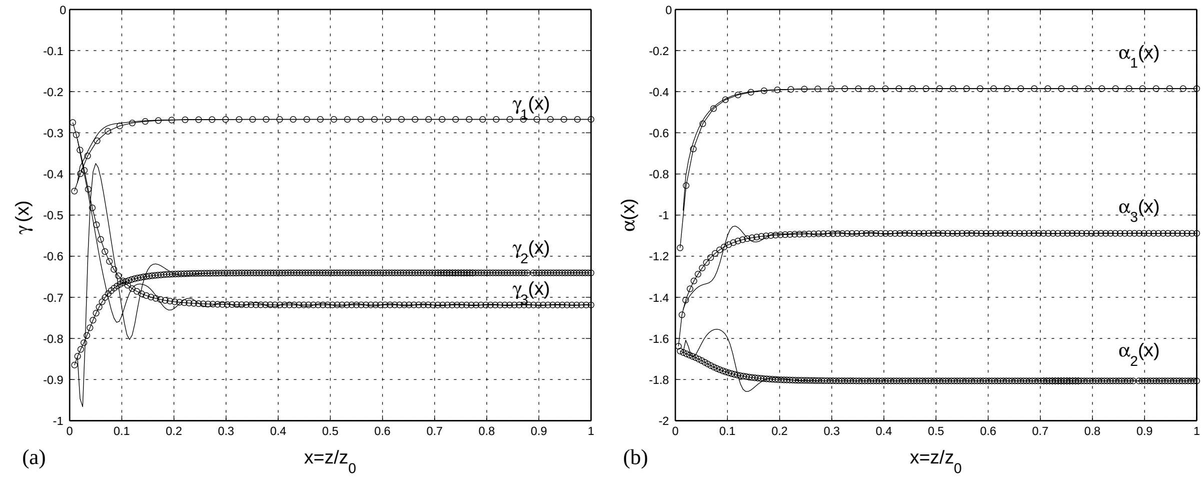


Fig. 2. $\gamma_{\mathrm{PSE}}(x)$ and $\gamma_{\mathrm{NP}}(x)$ (lines with circles). (b): $\alpha_{\mathrm{PSE}}(x)$ and $\alpha_{\mathrm{NP}}(x)$ (lines with circles). $Re = 100$, $L = 0.5$, $\Delta^{-1} = 100$, $\omega = -1$, $n = -1$; $x_0 = 0.015$, $\delta x = 0.005$. The axial evolution of the three less stable modes are shown.

three modes far downstream, being the second less stable mode at $x_0$ the one that becomes less stable far downstream (which, therefore, is the one given in Fernandez-Feria and del Pino, 2002; see, e.g., Fig. 5 of that reference). This switching between the less stable modes along the pipe is a common feature of almost all the cases considered below, so that it is not enough to consider the axial evolution of the less stable mode at $x = x_0$, but it is necessary to follow the axial evolution of several initial modes. Also observed in that figure is that the asymptotic values are practically reached at $x \simeq 0.2$, where the flow becomes a Hagen-Poiseuille flow with superimposed solid-body rotation. Fig. 2 also displays the functions $\gamma_{\mathrm{PSE}}(x)$ and $\alpha_{\mathrm{PSE}}(x)$ obtained from the PSE (29) when the axial integration is started at $x = x_0 = 0.015$ with the near-parallel eigenvalues of (39) for the three different modes just described (continuous lines; $\delta x = 0.005$ in the numerical integration). It is seen that these functions undergo large fluctuations before reaching the downstream asymptotes, except for the mode that becomes the less stable one downstream. These fluctuations are due to the axial switching between the eigenvalues of the operator $\mathbf{L}$ in (29). However, the fact that the functions $\gamma_{\mathrm{PSE}}(x)$ and $\alpha_{\mathrm{PSE}}(x)$ corresponding to the initial mode that eventually becomes the less stable one downstream have not noticeable fluctuations guarantees that the PSE would yield physically relevant information about the stability of the flow. This fact is a common feature of all the cases considered below. It must be added that the PSE results, in addition of being physically more precise than the near-parallel ones from Eq. (39) (because the axial history of the perturbations is taken into account), are considerably less costly to obtain numerically: the CPU time to obtain the whole curve $\gamma_{\mathrm{PSE}}(x)$ shown in Fig. 2 is of the order of the CPU time to obtain a single point of $\gamma_{\mathrm{NP}}(x)$.

Some comments on the accuracy of the PSE results are in order here. All the results given in this paper are obtained with $\delta x$=0.005, which is the smallest value allowed by the numerical stability of the PSE method, after using the stabilisation technique of Anderson et al. (1998). This value of $\delta x$ is small enough to obtain the axial evolutions $\gamma(x)$ and $\alpha(x)$ of the mode that eventually becomes the less stable one (the physical mode) with four or five significant figures, as shown by

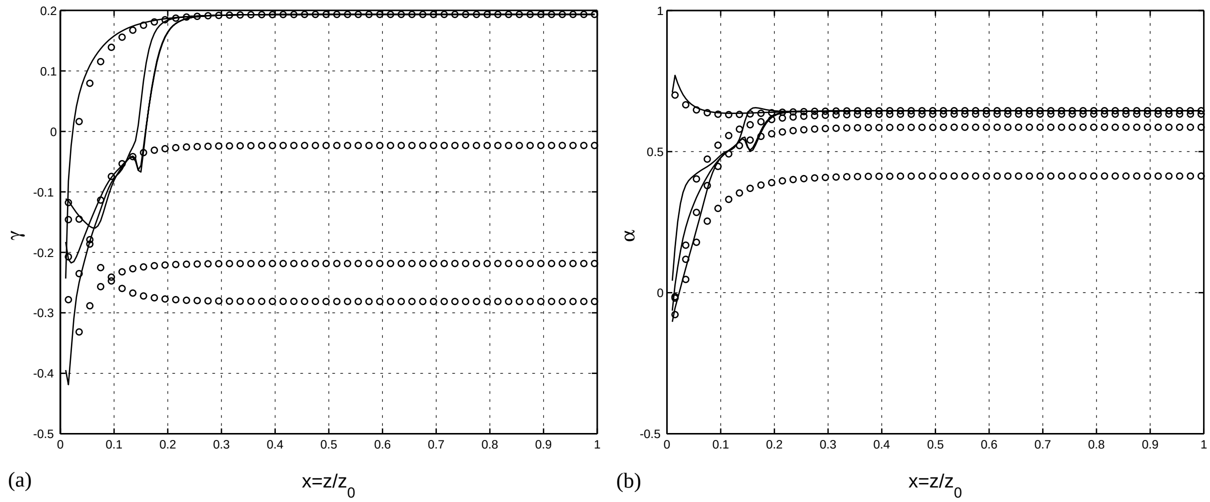


Fig. 3. As in Fig. 2, but for $Re = 500$, $L = 0.5$, $\Delta^{-1} = 400$, $\omega = -0.1$, $n = -1$; $x_0 = 0.01$, $\delta x = 0.005$ and the four less stable modes.

the results obtained with $\delta x = 0.006$, 0.007 and 0.01. However, the axial evolution of the fluctuating, nonphysical modes changes significantly as $\delta x$ increases, showing that some details of this behaviour are just numerical. Thus, the use of different values of $\delta x$ is relevant not only to check the accuracy of the results, but also to discard nonphysical modes. The same may be said in relation to the starting location $x_0$ (we have selected $x_0 = 0.01$ in all the shown computations): the axial evolution of the physically relevant (less stable) mode becomes independent of $x_0$ as $x_0$ decreases. However, the details of the evolution of the fluctuating, more stable, modes depend on this numerical parameter.

The difference between $\gamma_{NP}(x)$ and $\gamma_{PSE}(x)$ for the physically relevant mode in Fig. 2 is actually very small, so that one would think that the only advantage of the PSE is merely computational. However, this is not so when the flow becomes unstable, as shown in Fig. 3. There, the case $Re = 500$, $L = 0.5$, in a pipe of length $\Delta^{-1} = 400$, for perturbations with $\omega = -0.1$, and $n = -1$, is considered. These values of $Re$ and $L$ correspond to one of the cases analyzed experimentally by Imao et al. (1992) (see next section). According to Fernandez-Feria and del Pino (2002), the downstream flow is unstable for these values of $\omega$ and $n$. Obviously, the downstream asymptotic values of $a_{PSE}$ and $a_{NP}$ coincide because both Eqs. (29) and (39) yield the same results when the axial derivative becomes negligible in (29). The results at the initial axial position $x = x_0 = 0.01$ are also the same because $a_{NP}$ is used as the initial condition for (29) at $x_0$. However, the axial evolution of $a$ is quite different in both cases, particularly near the axial position where the flow becomes unstable ($\gamma = 0$). Therefore, the predictions about the instability of the flow, i.e. about the axial location where the flow becomes unstable, and about the frequency, wavelength and azimuthal wavenumber of the perturbation that first becomes unstable, are very different in both formulations. This can be better appreciated in Fig. 4, where the stability properties of this flow ($Re = 500$, $L = 0.5$) according to both formulations are compared for a wide significant range of frequencies, and for $n = -1$ and $-2$. For perturbations with $n = -1$, the flow becomes unstable at $x/\Delta \equiv z/R \simeq 12$ for

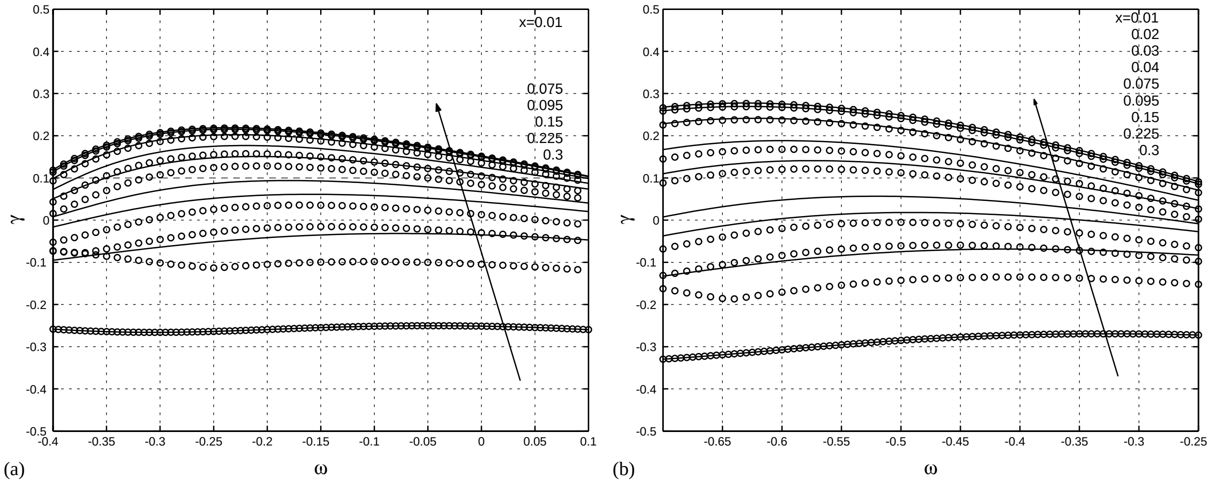


Fig. 4. Comparison between $\gamma_{\mathrm{PSE}}$ (continuous lines) and $\gamma_{\mathrm{NP}}$ (dots) for different values of $x$ (as indicated) as functions of $\omega$, for perturbations with $n=-1$ (a), and $n=-2$ (b), in a rotating flow with $Re=500$, $L=0.5$, $\Delta^{-1}=400$.

$\omega \simeq -0.15$ according to NP equation (39), and at $z/R \simeq 10$ for $\omega \simeq -0.1$ according to PSE (29). For perturbations with $n=-2$, $z/R \simeq 16$, $\omega \simeq -0.5$ according to (39), and $z/R \simeq 12.4$, $\omega \simeq -0.47$ according to (29).

Therefore, it is concluded that the use of the PSE is essential to correctly characterize the onset of linear instability of the flow. For this reason, all the results given below are obtained using this formulation (except specified otherwise).

Before finishing this section, it is of interest to present PSE results for the case of a swirless flow ($L=0$). As it is well known, the Hagen-Poiseuille flow is always linearly stable (e.g. Cotton and Salwen, 1981). In addition, since there is no azimuthal velocity component, the stability results are symmetric with respect to $\omega$=0, for a given $n$. Fig. 5 shows $\gamma(\omega)$ for $Re=500$, $n=-1$ and $-2$, for different values of $x$. Only the less stable mode is shown. The difference between $\gamma_{\mathrm{NP}}$ and $\gamma_{\mathrm{PSE}}$ is as important as in Fig. 4 for $L=0.5$, but now this has no physical consequences on the flow because all the perturbations are stable. The axial evolutions of the less stable mode obtained with both formulations for $\omega=-0.06$ are compared in Fig. 6.

### 4.2. Comparison between PSE results and experimental results

In this section we consider three of the cases that were analyzed experimentally by Imao et al. (1992) with more detail. Using laser doppler anemometry, these authors characterized the appearance of helical waves in the flow in an axially rotating pipe for $Re$=500 and several values of $L$. The flow developed from an uniform velocity profile at the inlet to rotating Hagen-Poiseuille flow downstream. However, at certain rotation rates, the flow fluctuated before this downstream state was reached, and they were able to characterize the frequency, axial wavelength, and azimuthal wavenumber of the spiral waves formed after instability of the basic flow.

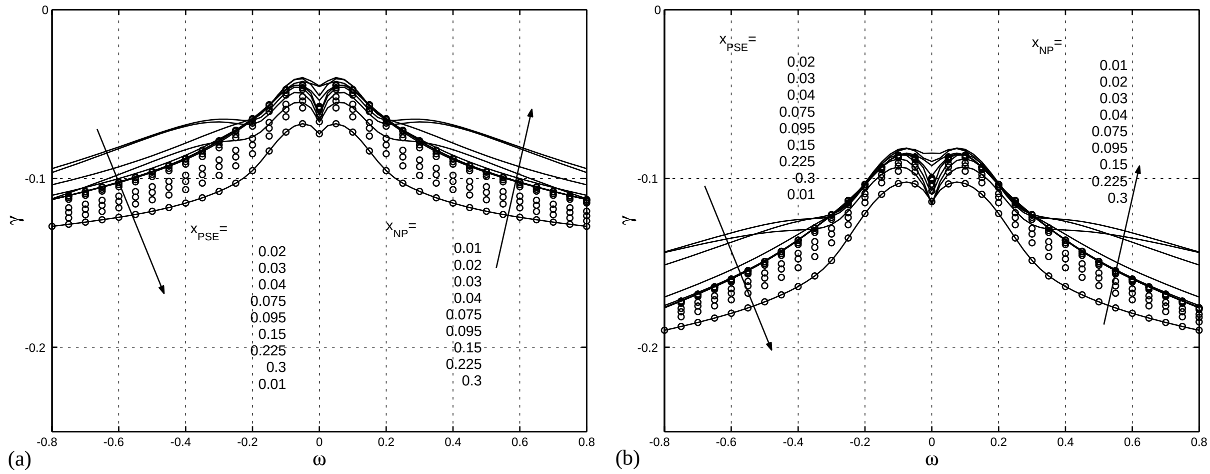


Fig. 5. Comparison between $\gamma_{\rm PSE}$ (continuous lines) and $\gamma_{\rm NP}$ (circles) for different values of $x$ (as indicated) as functions of $\omega$, for perturbations with $n=-1$ (a), and $n=-2$ (b), in a swirless flow ($L=0$) with $Re=500$, and $\Delta^{-1}=400$.

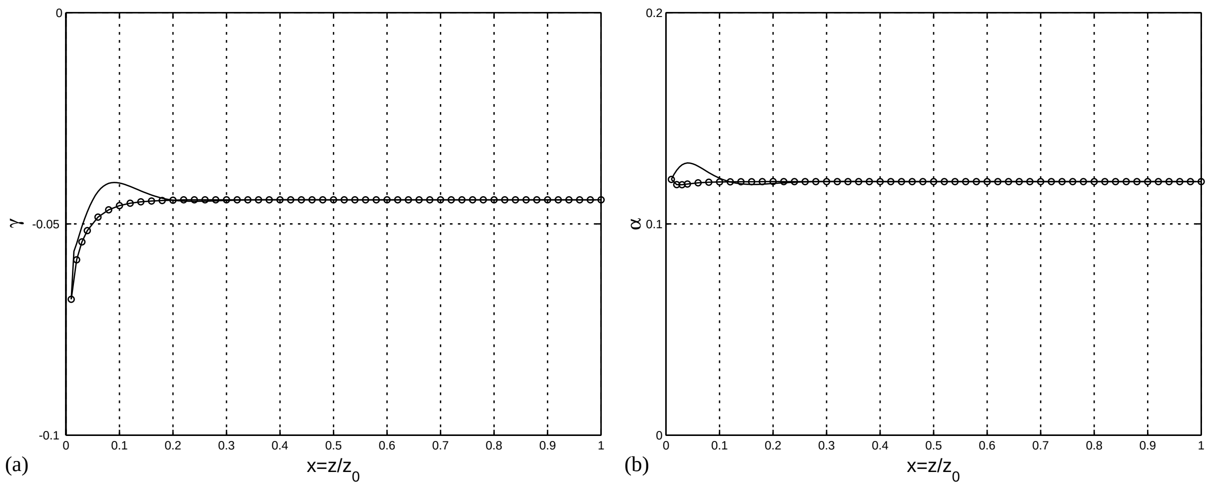


Fig. 6. (a): $\gamma_{\rm PSE}(x)$ and $\gamma_{\rm NP}(x)$ (lines with circles). (b): $\alpha_{\rm PSE}(x)$ and $\alpha_{\rm NP}(x)$ (lines with circles). $Re=500$, $L=0.0$, $\Delta^{-1}=400$, $\omega=-0.06$, $n=-1$; $x_0=0.01$, $\delta x=0.005$. Only the less stable mode is shown.

### 4.2.1. $Re=500$ and $L=0.5$

PSE results for this case have already been shown in Figs. 3 and 4. Fig. 7 shows the isocontours of $\gamma$ and $\alpha$ on the $(x,\omega)$-plane of the most unstable mode for $n=-1$ and $-2$. The length of the pipe used in the numerical simulation of the basic flow was $\Delta^{-1}=400$ (note that the abscissas in Fig. 7 is $x/\Delta=z/R$). The axial location at which the flow becomes unstable is better appreciated in Fig. 8(a), where the maximum values of $\gamma$ along the pipe are plotted for $n=-1$ and $-2$. The corresponding frequencies and the axial wavenumbers are plotted in Fig. 9. These results show that the flow becomes unstable quickly, much before the downstream asymptotic flow is reached.

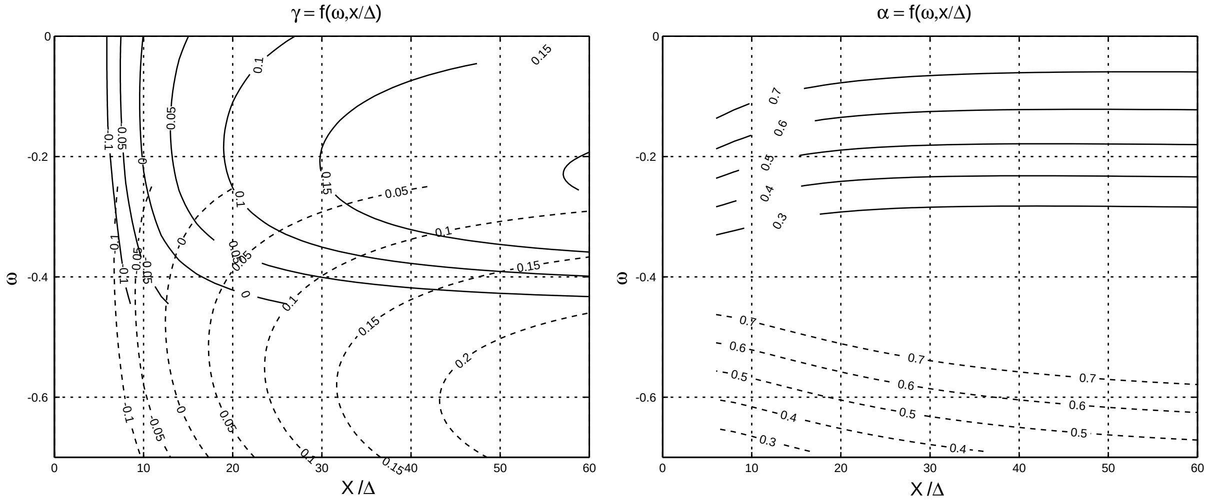


Fig. 7. Isocontours $\gamma = constant$ (a), and $\alpha = constant$ (b) on the $x/\Delta, \omega$ plane for the most unstable modes corresponding to $n = -1$ (continuous lines) and $n = -2$ (dashed lines). $Re = 500$, $L = 0.5$, $\Delta^{-1} = 400$, $\delta x = 0.005$, $x_0 = 0.01$ $(x_0/\Delta = 4)$.

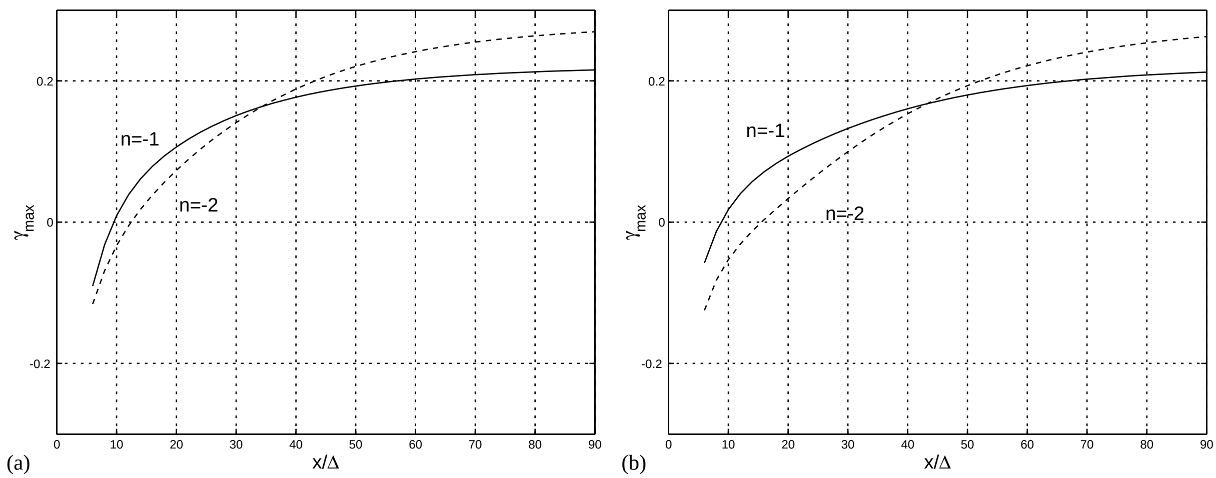


Fig. 8. (a): Maximum values of $\gamma$ as functions of $z/R$ corresponding to the cases plotted in Fig. 7. (b): The same results but for a basic flow with Hagen-Poiseuille flow at the inlet.

In particular, the mode with $n = -1$ is the first to become unstable, at $z/R \simeq 9.6$ (see Fig. 8(a)), for a frequency $\omega \simeq -0.1$, and an axial wavenumber $\alpha \simeq 0.72$ (see Fig. 9). However, the mode with $n = -2$ becomes unstable just after the $n = -1$ one, at $z/R \simeq 11.8$, with a growth rate that surpasses that of the mode $n = -1$, becoming the most unstable mode in the downstream solid-body rotating flow (see Fig. 8(a)). The corresponding frequency and axial wavenumber of this mode $n = -2$ when it becomes unstable at $z/R \simeq 12.4$ are $\omega \simeq -0.47$ and $\alpha \simeq -0.72$, respectively (Fig. 9).

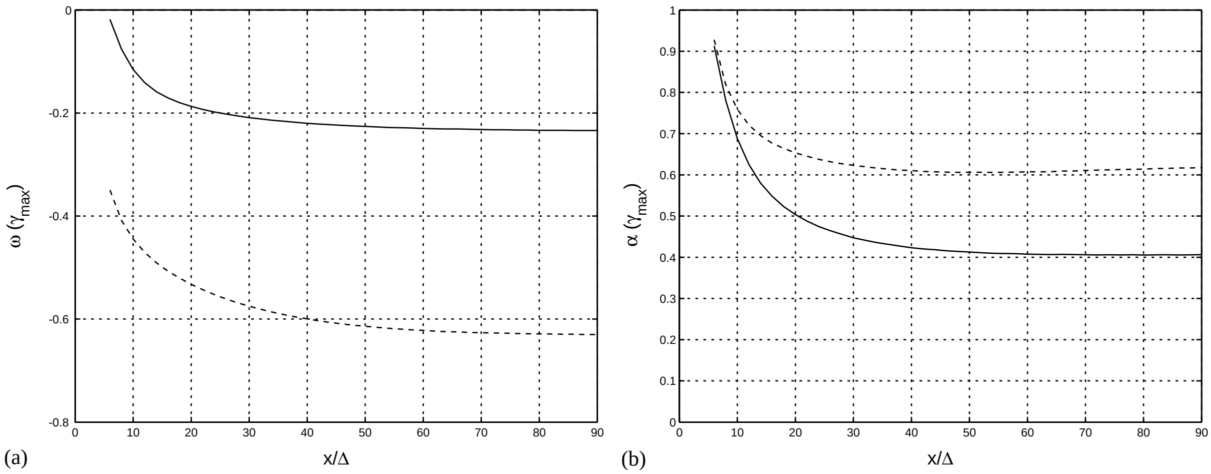


Fig. 9. Values of the frequency (a) and the axial wavenumber (b) corresponding to the growth rates plotted in Fig. 8(a).

The experimental results of Imao et al. (1992) for this case $Re=500$ and $L=0.5(Re_z=500,\ N=1$ in their notation) show that the flow becomes unstable before reaching the downstream rotating state. In particular, at $z/R=60$ these authors characterize a spiral wave (which is first detected slightly before $z/R=30$) superimposed to the basic flow with an azimuthal wavenumber $|n|=2$, a frequency which approximately coincides with the rotation frequency of the pipe, and a wavelength about eight times the pipe diameter, which in our notation corresponds to $\omega \simeq -0.5$ and $\alpha \simeq 0.78$, respectively. These two last values are very close to the theoretical ones found with the PSE for $n=-2$. However, there are two important discrepancies: the PSE predicts that the first mode to become unstable is $n=-1$, instead of $n=-2$, and the axial location for instability predicted by the PSE is quite upstream of the experimental value $z/R \simeq 30$. It must be admitted that there exists some uncertainty in the axial location for instability measured experimentally, because the perturbation has to evolve some distance downstream, after its growth rate has become positive, before being measurable. In addition, the PSE results show that the growth rate for $n=-2$ increases with $x$ faster than the growth rate for $n=-1$, surpassing it at $z/R \simeq 33$ (Fig. 8(a)), so that at $z/R=60$, where the experimental spiral wave is described, the most unstable mode corresponds to $n=-2$. These two circumstances may explain why the spiral wave observed experimentally corresponds to $n=-2$, with that good agreement between the experimental and theoretical frequencies and axial wavenumbers ($\omega \simeq -0.5$ and $\alpha \simeq 0.78$ in the experiments, and $\omega \simeq -0.47$ and $\alpha \simeq 0.72$ with the PSE).

In Figs. 8(b) and 10 we have included results obtained for the same flow parameters ($Re=500$, $L=0.5$) but with different inlet conditions of the basic flow. Instead of uniform axial velocity at the inlet we have considered the case in which the flow enters the pipe with the Hagen-Poiseuille velocity profile already formed, but, of course, without rotation, which develops along the pipe. This inlet condition does not correspond to the experimental setup of Imao et al. (1992), but it is interesting to see how the stability results change with the inlet conditions. It is observed that the results for $n=-1$ are very similar. However, there are important differences for $n=-2$, particularly for the axial wavenumber (compare Fig. 10(b) with Fig. 9(b)), and for the location where the flow first becomes unstable (compare Fig. 8(a) with Fig. 8(b)).

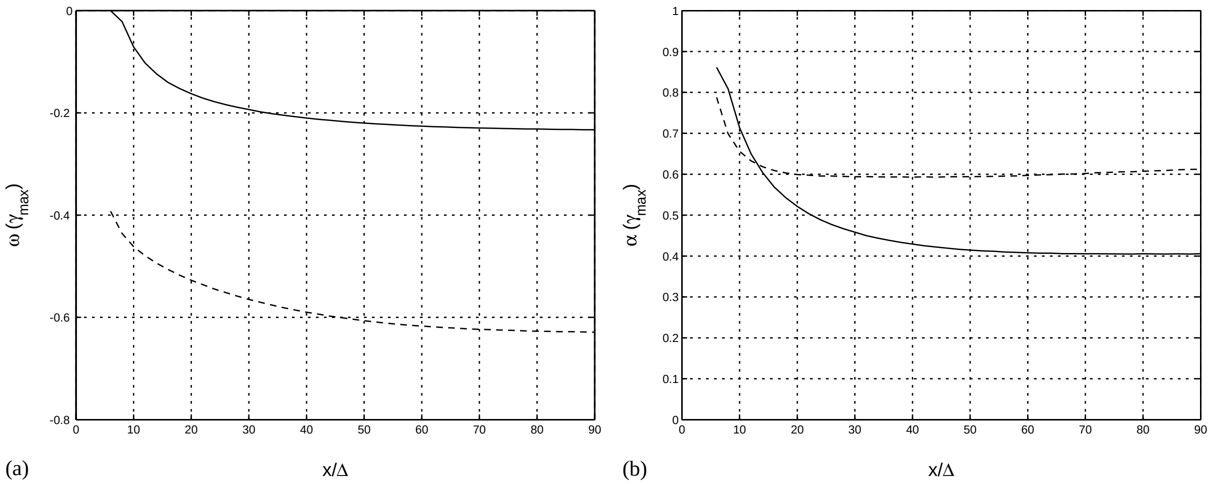


Fig. 10. Values of the frequency (a) and the axial wavenumber (b) corresponding to the growth rates plotted in Fig. 8(b).

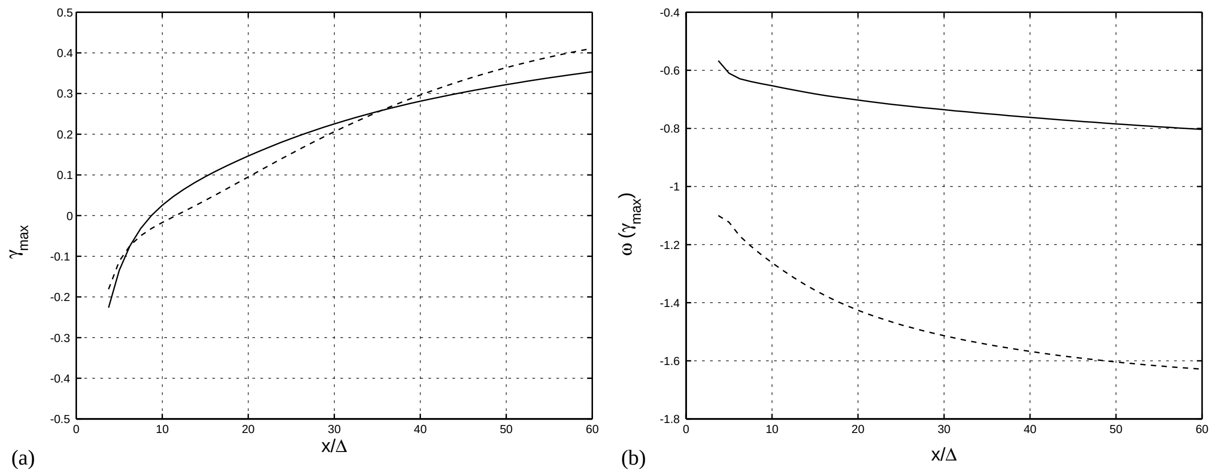


Fig. 11. (a) Maximum values of $\gamma$ as functions of $z/R$ for $Re = 500$ and $L = 1$, and their corresponding frequencies (b). Continuous lines are for $n = -1$ and dashed lines for $n = -2$.

### 4.2.2. $Re = 500$ *and* $L = 1$

The above described shift between $n = -1$ and $-2$ modes is more evident for $L = 1$. For this rotation rate, Imao et al. (1992) report ($L = 1$ corresponds to $N = 2$ in their notation) that the two kinds of spiral waves ‘appear alternately’. The PSE results show that maximum values of the growth rates for the modes $n = -1$ and $-2$ are in fact very close to each other all along the pipe [Fig. 11(a)]. Moreover, the frequencies corresponding to $\gamma = 0$ for $n = -1$ and $-2$ are both in agreement with the experimental results: Imao et al. find that $|\omega/n| \simeq 0.7$, which agree quite well with the PSE results $\omega \simeq -0.65$ for $n = -1$, and $\omega \simeq -1.3$ for $n = -2$ [see Fig. 11(b)].

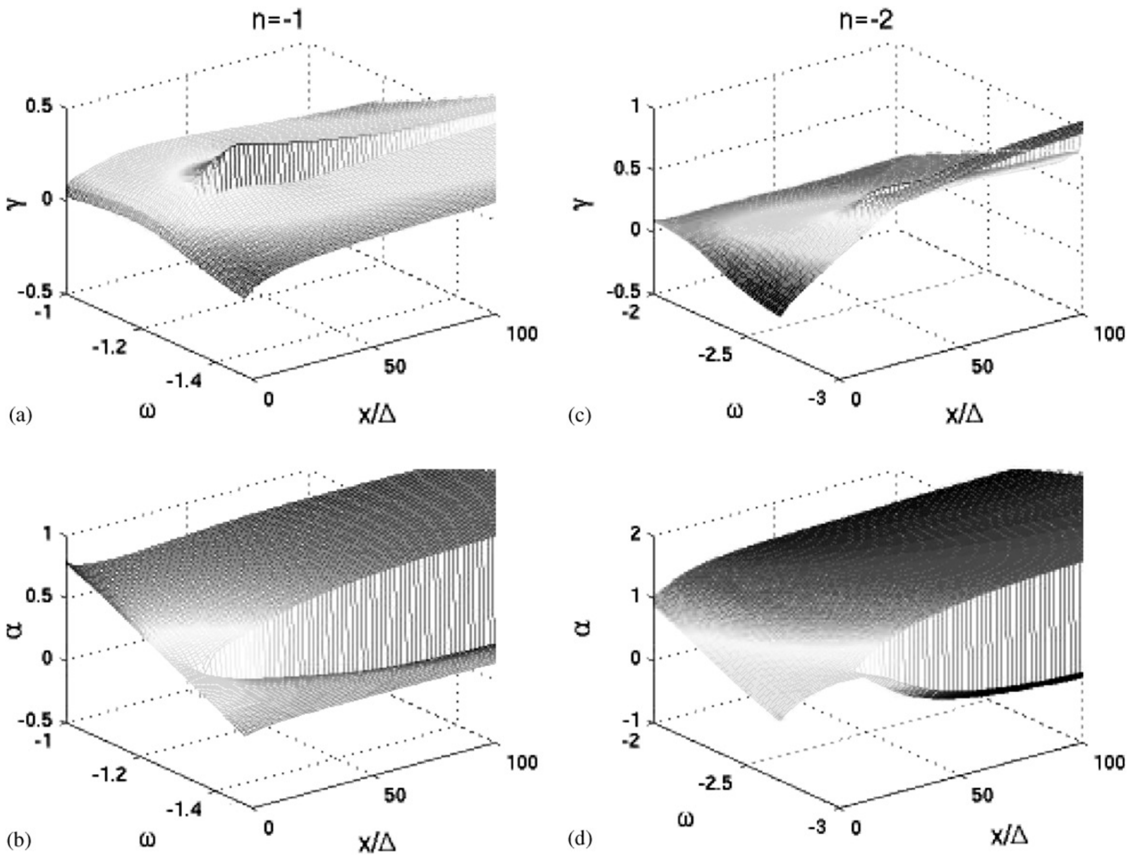


Fig. 12. Surfaces $\gamma(\omega, x/\Delta)$ and $\alpha(\omega, x/\Delta)$ for $Re = 500$, $L = 1.5$. $n = -1$ [(a) and (b)], and $n = -2$ [(c) and (d)]. $x_0 = 0.01$ ($x_0/\Delta = 4$), $\delta x = 0.005$.

#### 4.2.3. $Re = 500$ and $L = 1.5$

Fig. 12 shows the surfaces $\gamma(\omega, x)$ and $\alpha(\omega, x)$ for the less stable modes with $n = -1$ and $-2$ obtained with the PSE for this case (the length of the pipe in the numerical simulation of the basic flow was $\Delta^{-1} = 400$). The maximum values of $\gamma$ along the pipe are plotted in Fig. 13 for $n = -1$ and $-2$. The corresponding values of the frequency and the axial wavenumber are plotted in Fig. 14. According to these figures, the flow first becomes unstable at $z/R \simeq 5.5$ for a perturbation with $n = -1$, $\omega \simeq -1.2$, and $\alpha \simeq 0.41$. The experiments of Imao et al. (1992) for this case ($Re_z = 500$, $N = 3$, in their notation) show that at $z/R \simeq 26$ there already exists an spiral wave with azimuthal wavenumber $|n| = 1$, with a frequency about 0.8 times the rotation frequency of the pipe, and a wavelength about ten times the pipe diameter, which in our notation corresponds to $\omega \simeq -1.2$ and $\alpha \simeq 0.32$, respectively. These experimental values of $n$, $\omega$ and $\alpha$ are then in very good agreement with those obtained with the PSE (as discussed above, the axial location where the spiral wave is first detected experimentally may be quite downstream the location where the growth rate $\gamma$ becomes positive).

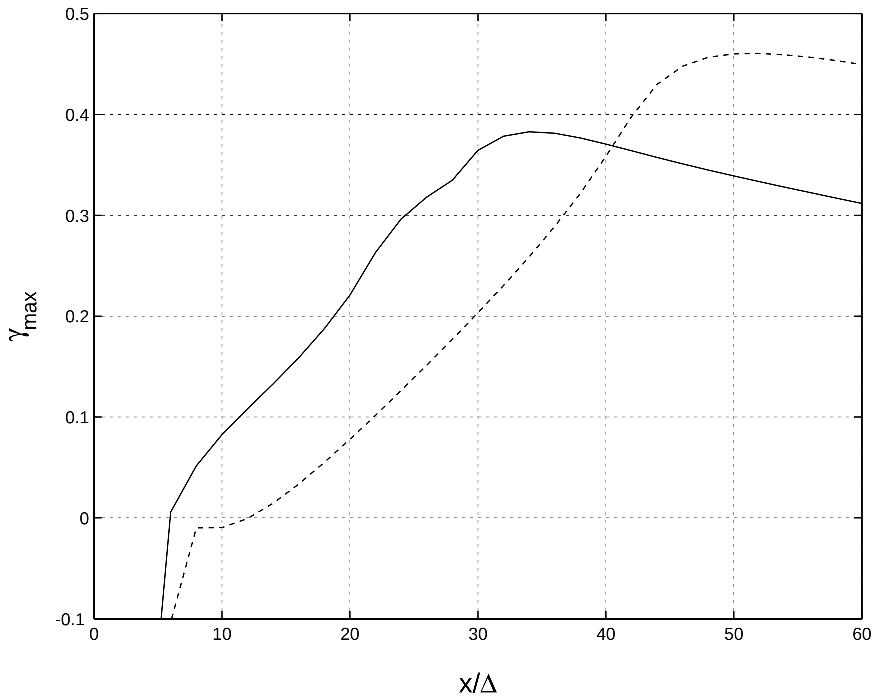


Fig. 13. Maximum values of $\gamma$ as functions of $z/R$ for $Re = 500$ and $L = 1.5$. The continuous line is for $n = -1$, and the dashed line for $n = -2$.

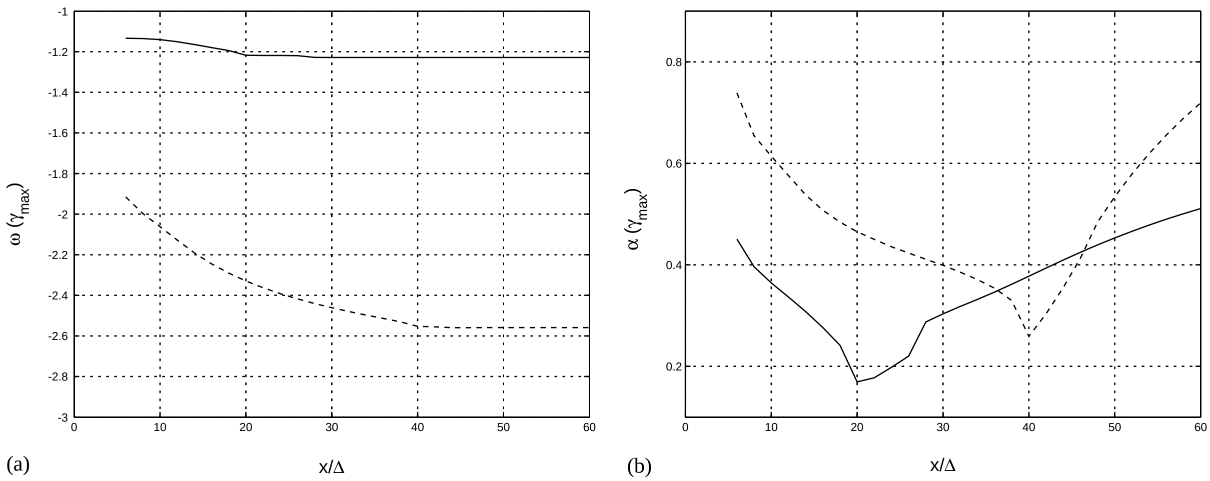


Fig. 14. Frequency (a) and axial wavenumber (b) corresponding to the functions $\gamma(x)$ plotted in Fig. 10. The continuous lines are for $n = -1$ and the dashed lines for $n = -2$.

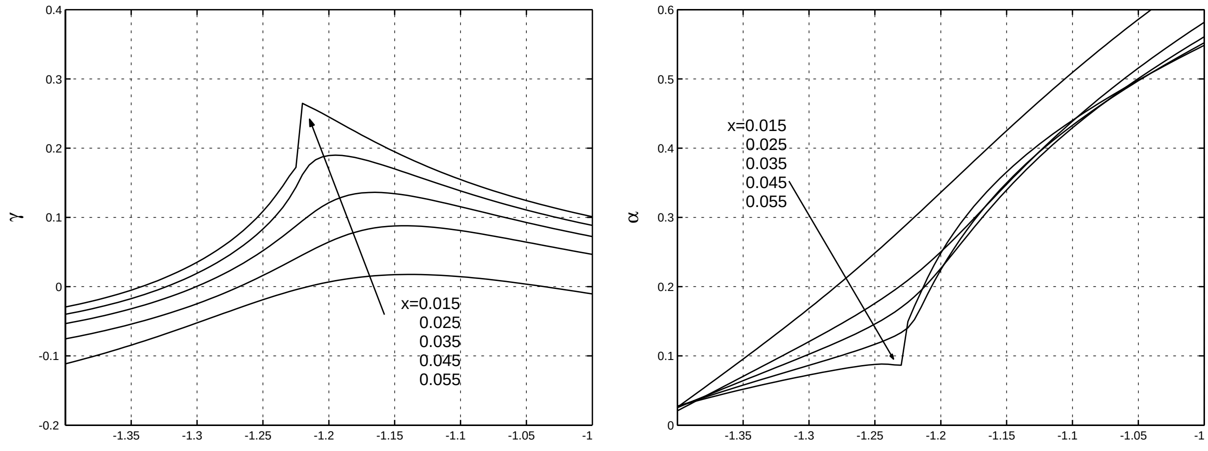


(a) (b)

Fig. 15. $\gamma(\omega)$ for several values of $x$ (a), and $\alpha(\omega)$ for the same values of $x$, for $Re = 500$, $L = 1.5$, and $n = -1$.

An important difference of the present case in relation to those considered in the previous sections is that the downstream rotating Hagen-Poiseuille flow for $Re$=500 and $L$=1.5 is not only convectively unstable, but also absolutely unstable (see Fernandez-Feria and del Pino, 2002, Figs. 10 and 11). Therefore, this case may serve to check whether the absolute instability appears before the asymptotic downstream flow is formed (like it occurs for the convective instabilities just described), and, in that case, to analyze the formation of an absolute instability in an axially developing flow. Actually, Fig. 12(b) for $n = -1$ shows that at $z/R \simeq 22$ ($x \simeq 0.055$) there exists a *saddle point* in the axial wavenumber function $\alpha(\omega, x)$ for $\omega \simeq -1.23$, which coincides with a *cusp point* of $\gamma(\omega, x)$ in Fig. 12(a) (remember that the convective instability for $n = -1$ appears quite upstream, at $z/R \simeq 5$). This behavior, which, according to the Briggs-Bers criterion may indicate the onset of absolute instability (see, e.g., Huerre and Monkewitz, 1990), is better appreciated in Fig. 15, where cross sections $\gamma(\omega)$ and $\alpha(\omega)$ of the surfaces depicted in Figs. 12(a)–(b) are plotted for several values of $x$. At $x \simeq 0.055$, both $\partial\alpha/\partial\omega$ and $\partial\gamma/\partial\omega$ become infinity at $\omega \simeq -1.23$, due to the saddle point of $\alpha$ and the cusp point of $\gamma$, respectively, so that the complex group velocity $v_g = \partial\omega/\partial\alpha + \mathrm{i}\partial\omega/\partial\gamma$ vanishes. This is a necessary, though not sufficient, condition for the absolute instability of the flow. Nevertheless, it was found in Fernandez-Feria and del Pino (2002), that the condition $v_g$=0 was always linked to the onset of absolute instability of the fully developed rotating Hagen-Poiseuille flow, so that one may think that this is also the case for the developing flow (it is not easy to characterize the merging of two spatial branches of the dispersion relation using the PSE formulation). If this is so, the flow becomes absolutely unstable before it is fully developed. A similar behavior appears for $n = -2$, but further downstream, at $z/R \simeq 44$ ($x \simeq 0.11$) for $\omega \simeq -2.56$ [see Figs. 12(c)–(d)]. However, the spatial stability analysis on which the PSE is based is no longer valid once the complex group velocity vanishes at $z/R \simeq 22$ for $n = -1$.

In relation to the experimental results of Imao et al. (1992), these authors report that the fluctuations appearing in this case with $L = 1.5$ are much more amplified than in the cases considered in the previous sections (at $z/R = 60$ the amplitude of the fluctuations amounts to 30 percent of the mean axial velocity!). This behavior may be related to the appearance of the absolute instability. Far downstream, however, the flow becomes turbulent. No vortex breakdown phenomenon is reported by Imao et al. (1992).

## 5. Conclusions

It has been shown that the use of parabolized stability equations (PSE) is a good and efficient tool for analyzing the nonparallel stability of the axially developing flow in a rotating pipe. Although the less stable mode at the pipe inlet does not coincide, in general, with the less stable mode downstream, the PSE always follow correctly the mode that becomes the less stable one downstream in the pipe. When the flow becomes (convectively) unstable (to nonaxisymmetric perturbations) it does so quite before reaching the asymptotic Hagen-Poiseuille flow with superimposed solid-body rotation, in agreement with previous experimental results by Imao et al. (1992). Actually, a good agreement with the experimental frequencies, axial and azimuthal wavenumbers of the unstable disturbances reported by these authors is found. The method is also appropriate for detecting one of the conditions characterizing the onset of absolute instability of the axially developing flow, which also appears before the downstream flow is fully developed. However, downstream the axial location where some perturbations have negative group velocities the spatial stability analysis on which the PSE method is based is no longer valid. From these results, we are confident that the method can be used for the stability analysis of more complex axially developing swirling flows of practical and theoretical interest.

## Acknowledgements

This research has been supported by the Ministerio de Ciencia y Tecnologí a of Spain (Grant No. BFM00-1323).

## References

Anderson, P., Henningson, D.S., Hanifi, A., 1998. On a stabilization procedure for the parabolic stability equations. J. Eng. Math. 33, 311–332.

Batchelor, G.K., Gill, A.E., 1962. Analysis of the stability of axisymmetric jets. J. Fluid Mech. 14, 529–551.

Bertolotti, F.P., Herbert, Th., Spalart, P.R., 1992. Linear and nonlinear stability of the Blasius boundary layer. J. Fluid Mech. 242, 441–474.

Bridges, T.J., Morris, P.J., 1984. Differential eigenvalue problems in which the parameter appears nonlinearly. J. Comput. Phys. 55, 437–460.

Cotton, F.W., Salwen, H., 1981. Linear stability of rotating Hagen-Poiseuille flow. J. Fluid Mech. 108, 101–125.

Fernandez-Feria, R., 1999. Nonparallel linear stability analysis of Long's vortex. Phys. Fluids 11, 1114–1126.

Fernandez-Feria, R., del Pino, C., 2002. The onset of absolute instability of rotating Hagen-Poiseuille flow: a spatial stability analysis. Phys. Fluids 14, 3087–3097.

Herbert, Th., 1997. Parabolized stability equations. Ann. Rev. Fluid Mech. 29, 245–283.

Imao, S., Zhang, Q., Yamada, Y., 1989. The laminar flow in the developing region of a rotating pipe. JSME Int. J. Ser. II 32, 317–323.

Imao, S., Itoh, M., Yamada, Y., Zhang, Q., 1992. The characteristics of spriral waves in an axially rotating pipe. Exp. Fluids 12, 277–285.
Khorrami, M.R., Malik, M.R., Ash, R.L., 1989. Application of spectral collocation techniques to the stability of swirling flows. J. Comput. Phys. 81, 206–229.
Lopez, J.M., Weidman, P.D., 1996. Stability of stationary endwall boundary layers during spin-down. J. Fluid Mech. 326, 373–398.
Mackrodt, P.A., 1976. Stability of Hagen-Poiseuille flow with superimposed rigid rotation. J. Fluid Mech. 73, 153–164.
Maslowe, S.A., 1974. Instability of rigidly rotating flows to non-axisymmetric disturbances. J. Fluid Mech. 64, 307–317.
Maslowe, S.A., Stewartson, K., 1982. On the linear inviscid stability of rotating Poiseuille flow. Phys. Fluids 25, 1517–1523.
Pedley, T.J., 1969. On the instability of viscous flow in a rapidly rotating pipe. J. Fluid Mech. 35, 97–115.
White, A., 1964. Flow of a fluid in an axially rotating pipe. J. Mech. Eng. Sci. 6, 47–52.